45th AIAA Aerospace Sciences Meeting and Exhibit
8 - 11 January 2007, Reno, Nevada

AIAA 2007-993

45th AIAA Aerospace Sciences Meeting, Jan 8–11, Reno, Nevada

Direct Numerical Simulation of the Thermal Effects in Plasma/Turbulence Interaction

Shankar Ghosh* and Krishnan Mahesh†

University of Minnesota, Minneapolis, MN, 55455, USA

The thermal effects of laser–induced plasma on isotropic turbulence are studied using direct numerical simulation. Laminar and turbulent simulations are conducted. For the laminar simulations, a tear–drop shaped blast wave propagates into the background becoming spherical in time. Shock radius and jumps in fluid properties at the shock front are compared to experiment. Both short and long time behavior of the plasma is studied. At short times, baroclinic vorticity is generated as a consequence of propagation of the curved shock through the domain. At long times, the flow field forms toroidal vortex rings, as observed in experiments. For the turbulent simulations, turbulence levels get enhanced in regions of compression across the blast wave and suppressed in regions of expansion in the plasma core.

I. Introduction

Laser energy deposition has been studied in great detail (e.g. Maker et al. 1963, Damon & Tomlinson 1963, Meyerand & Haught 1963). Applications of laser–induced breakdown of a gas include localized flow control of supersonic flows (Adelgren et al 2003), drag reduction in supersonic and hypersonic flows (Riggins 1999), ignition of combustion gases (Phuoc 2000) and providing thrust to aerospace vehicles (Molina-Morales et al 2001, Wang et al 2001).

When a laser beam is focused on a small volume of gas, the gas molecules in the focal volume absorb energy and get ionized. The plasma formation process involves multiple steps. The initial release of electrons is due to multi–photon ionization, which requires that multiple photons are incident on an atom simultaneously. Multiple photons are needed since ionization energies for most gases are larger than the energy of a single photon in the laser beam. During this process, the electron number density increases linearly in time. The released electrons in the focal volume absorb laser energy due to inverse bremsstrahlung absorption, where a free electron in presence of a third body, absorbs energy and gets excited. Many such interactions are needed for the electron to gain sufficient energy to impact ionize neutral atoms. The resultant electron concentration increases exponentially in time. The plasma thus formed, absorbs laser energy and spreads out in the direction of the laser beam due to a combination of absorption and reflection. The highly ionized plasma in the focal volume reflects part of the laser energy incident on it. This energy is absorbed by adjacent molecules, in the direction of the laser beam. These molecules get ionized, and start reflecting laser radiation. This process continues until the plasma has spread out and assumed a tear–drop shape. The energized electrons collide with the heavy particles leading to heating of the gas. Also due to these collisions, the electrons get de–energized and recombine with ions, sharply decreasing the electron number

*Graduate Research Assistant

†Associate Professor

density. Thus an energy spot with temperature and pressure higher than that of the surroundings is left at the end of the plasma formation process. The sharp pressure gradients lead to formation of a blast wave that propagates into the background gas.

Recent experimental work on pulsed laser induced breakdown in quiescent air or nitrogen, include Jiang et al. (1998), Lewis et al. (1999) and Adelgren et al. (2001). Jiang et al. (1998) used a laser beam of 1.38 J focused on a 3 mm diameter spherical region to cause breakdown in air. The laser was pulsed for a duration of 18 nanoseconds. Adelgren et al. (2001) used a Nd:YAG laser of 200 mJ pulsed for 10 nanosecond duration in air. The experimental data show a wide separation in time–scales between the laser pulse duration and observations of the blast wave propagation. As seen above, the laser is pulsed on a time–scale of 10 nanoseconds. The blast wave, on the other hand is observed on a time–scale of 10 to 100 microseconds. Since plasma formation is on a time–scale of the same order as the laser pulse duration, the three to four order of magnitude separation in time–scale suggests that the plasma may be considered to be formed instantaneously to a first approximation, to evaluate its gas–dynamic effect on the surrounding fluid. Brode (1955) performed a numerical simulation of the blast wave and concluded that the ideal gas assumption was reasonable for shock pressures less than 10 atmospheres in air. Steiner et al. (1998) perform computations using a real gas model to show that, when initialized with a self similar strong shock solution, the shock radius in the real gas model is quite close to that predicted by the classical point source explosion in an ideal gas. Other computations of blast wave propagation in quiescent air include those by Jiang et al (1998) and Yan et al. (2003). Dors et al. (2000) present a computational model which considers the asymmetry of laser energy deposition as well as ionization and dissociation effects on fluid properties. The initial stages of plasma formation due to laser energy deposition were modeled by Kandala and Candler (2002).

This paper considers generation of laser induced plasma in quiescent air and in background isotropic turbulence. Local thermodynamic equilibrium conditions are assumed to apply. Only thermal effects of the plasma are considered. A Fourier spectral solver has been developed for the simulations. The solver assumes periodic boundary conditions. The flow field resulting from laser energy deposition is axisymmetric and non–stationary in time. Periodic boundary conditions would work fine as long as the blast wave does not touch the domain boundaries. This is because if the blast wave is well resolved, the gradients ahead of it will be zero.

II. Simulation methodology

A. Algorithm description

The governing equations are the continuity and compressible Navier–Stokes equations,

$$\frac{\partial \rho}{\partial t} + \frac{\partial \rho u_i}{\partial x_i} = 0, \tag{1}$$

$$\frac{\partial \rho u_j}{\partial t} + \frac{\partial \rho u_j u_i}{\partial x_i} = -\frac{\partial}{\partial x_i}\left[p\delta_{ij} - \frac{\mu(T)}{Re}\left(\frac{\partial u_i}{\partial x_j} + \frac{\partial u_j}{\partial x_i} - \frac{2}{3}\frac{\partial u_k}{\partial x_k}\delta_{ij}\right)\right], \tag{2}$$

$$\frac{\partial \rho e_T}{\partial t} + \frac{\partial \rho e_T u_i}{\partial x_i} = \frac{\partial}{\partial x_i}\left[-pu_i + \frac{\mu(T)}{Re}\left(\frac{\partial u_i}{\partial x_j} + \frac{\partial u_j}{\partial x_i} - \frac{2}{3}\frac{\partial u_k}{\partial x_k}\delta_{ij}\right)u_j\right] + \frac{\partial}{\partial x_i}\left(\frac{\kappa(T)}{(\gamma-1)RePr}\frac{\partial T}{\partial x_i}\right) \tag{3}$$

where all the variables are non–dimensionalized with respect to their initial background values.

$$x_i = {x_i}^*/{L_0}^*, \qquad u_i = {u_i}^*/{c_0}^*, \qquad t = t^*{c_0}^*/{L_0}^*, \tag{4}$$

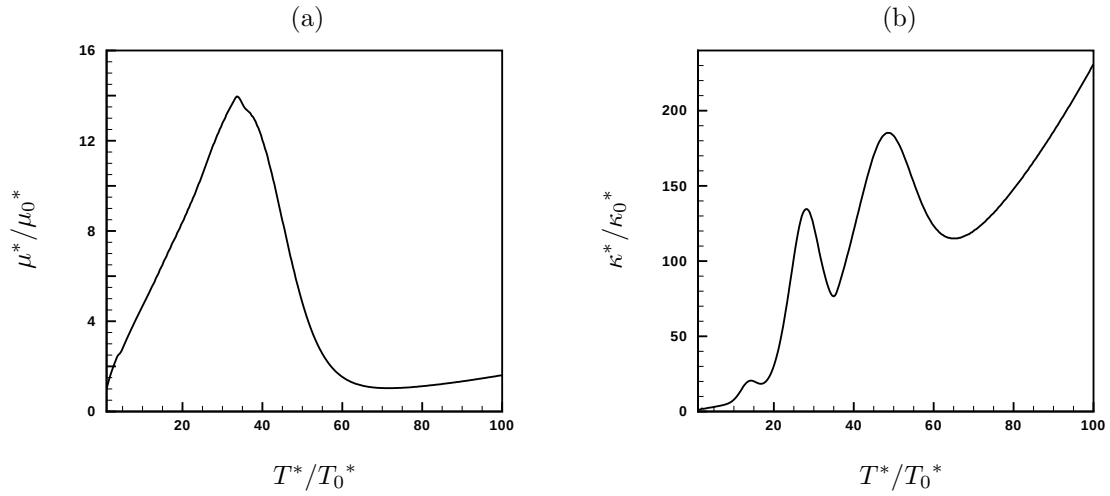

Figure 1. (a) Variation of the coefficient of viscosity μ with temperature T. (b) Variation of the coefficient of thermal conductivity κ with temperature T.

$$\rho = \rho^*/{\rho_0}^*, \qquad p = p^*/{\rho_0}^*{c_0}^{*2}, \qquad T = T^*/{T_0}^*$$
$$\mu(T) = \mu(T)^*/{\mu_0}^*, \qquad \kappa(T) = \kappa(T)^*/{\kappa_0}^*.$$

Here, the subscript '0' denotes initial background values and the superscript, '*' denotes dimensional variables. L_0^* is the length scale and is obtained by comparing the non–dimensional length of the plasma region used in the simulations to the actual dimensional length of the plasma. c_0^* is the speed of sound based on initial background temperature; i.e.

$$ {c_0}^* = (\gamma R^* {T_0}^*)^{1/2}. \tag{5}$$

$\mu(T)^*$ and $\kappa(T)^*$ are dimensional coefficients of viscosity and thermal conductivity obtained by assuming an equilibrium model for air (figure 1). The equation of state is given by

$$p = \rho T/\gamma, \tag{6}$$

where the temperature is related to the internal energy as

$$T = \gamma(\gamma - 1)e, \tag{7}$$

and the total energy is related to internal energy and kinetic energy as

$$\rho e_T = \rho e + \frac{1}{2}\rho u_i u_i. \tag{8}$$

The Reynolds number and Prandtl number are given by

$$Re = {\rho_0}^* {c_0}^* {L_0}^*/{\mu_0}^*, \quad Pr = {\mu_0}^* {c_{p0}}^*/{\kappa_0}^*. \tag{9}$$

${c_{p0}}^*$ is the specific heat at constant pressure at $T^* = {T_0}^*$.
The Navier–Stokes equations are solved using Fourier methods to compute the spatial derivatives. Any variable f is discretely represented as

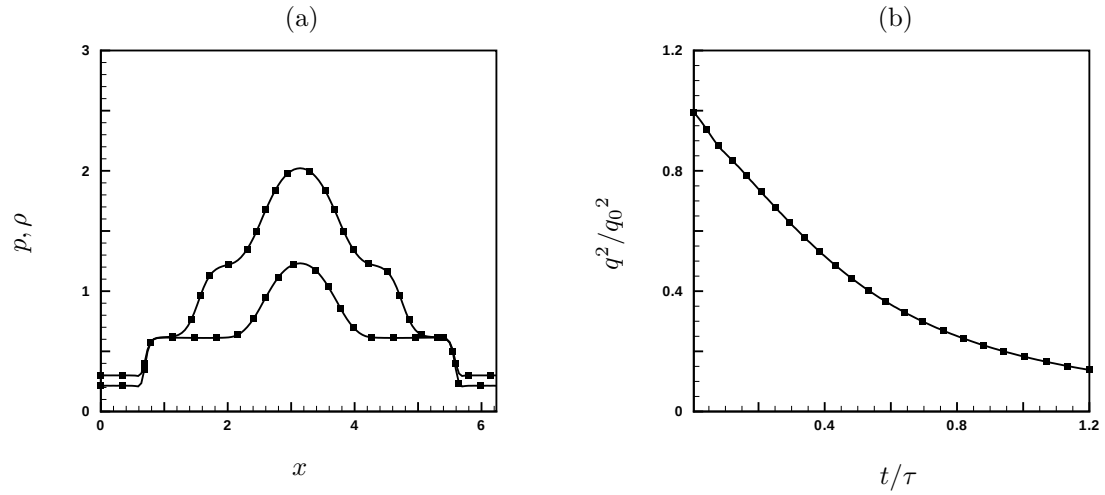

Figure 2. (a) Comparison of profiles for the periodic shock tube problem at $t = 1.0$, ——— without shock capturing and $\log\rho$ formulation, ■ with shock capturing and $\log\rho$ formulation, (b) Decay of turbulent kinetic energy for isotropic turbulence. Time is non–dimensionalized by the eddy turn over time τ, ——— without $\log\rho$ formulation, ■ with $\log\rho$ formulation.

$$f(x_1,x_2,x_3) = \sum_{k_1=-N_1/2}^{N_1/2-1} \sum_{k_2=-N_2/2}^{N_2/2-1} \sum_{k_3=-N_3/2}^{N_3/2-1} \hat{f}(k_1,k_2,k_3) \mathrm{e}^{(k_1x_1+k_2x_2+k_3x_3)} \tag{10}$$

where $\hat{f}(k_1,k_2,k_3)$ are the Fourier coefficients of f, and N_1, N_2 and N_3 are the number of points used to discretize the domain along x_1, x_2 and x_3 respectively. The Fourier coefficients of the spatial derivatives are therefore

$$\widehat{\frac{\partial f}{\partial x_\alpha}} = ik_\alpha \widehat{f}, \quad \widehat{\frac{\partial^2 f}{\partial x_\alpha x_\alpha}} = -k_\alpha^2 \widehat{f}. \tag{11}$$

A collocated approach is used, and the solution is advanced in time using a fourth order Runge–Kutta scheme. The skew–symmetric form of the convection terms

$$\frac{\partial fg}{\partial x_j} = \frac{1}{2}\left[\frac{\partial fg}{\partial x_j} + f\frac{\partial g}{\partial x_j} + g\frac{\partial f}{\partial x_j}\right], \tag{12}$$

is used to suppress aliasing errors resulting from the nonlinear convection terms (Blaisdell 1991). The above algorithm is implemented for parallel platforms using MPI. The library FFTW is used to compute Fourier transforms, and a pencil data structure is used. Each processor stores data along the entire extent of the x_1- direction, while data along the x_2- and x_3- directions are equally distributed among the processors. Fourier transforms along the x_1- direction are therefore readily computed, while transforms in the other directions require that the data be transposed prior to transforming.

B. Shock capturing

Recall that a strong shock wave propagates through the flow domain, when energy is added instantaneously. Experiments in laser induced breakdown (Yan et al 2003) show that the maximum temperature in the core is very high. This leads to sharp gradients in the flow variables. Since the flow solver uses spectral methods for

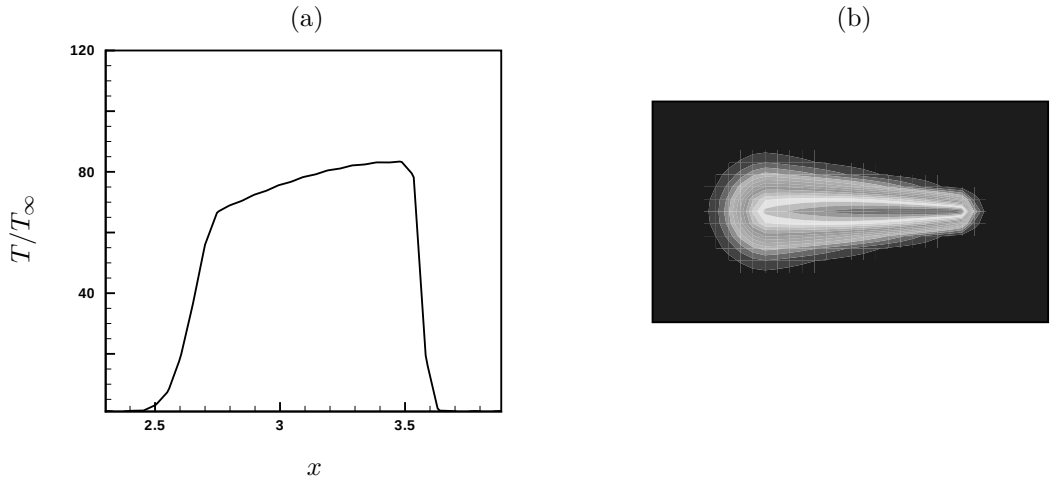

Figure 3. (a) Axial variation of the initial temperature profile, (b) Contour plot of initial temperature in a plane through the plasma axis.

spatial discretization, resolving these sharp gradients requires a highly refined mesh. The computational cost therefore increases significantly with increasing core temperatures. The Fourier spectral method is therefore combined with a shock capturing scheme proposed by Yee et al (1999), to avoid resolution of the shock thickness.

The shock capturing scheme is based on the finite volume methodology, and is applied as a corrector step to the Fourier discretization used in this paper. In the first step, the predicted form of the solution vector is obtained using Fourier methods as discussed in section A. This solution vector is then corrected using the filter numerical fluxes obtained by using a characteristic based filter

$$U^{n+1} = \widehat{U}^{n+1} + \Delta t \left[\frac{1}{\Delta x}\left(\widetilde{F}^{\star}_{i+1/2,j,k} - \widetilde{F}^{\star}_{i-1/2,j,k}\right) + \right. \tag{13}$$

$$\left. \frac{1}{\Delta y}\left(\widetilde{G}^{\star}_{i,j+1/2,k} - \widetilde{G}^{\star}_{i,j-1/2,k}\right) + \frac{1}{\Delta z}\left(\widetilde{H}^{\star}_{i,j,k+1/2} - \widetilde{H}^{\star}_{i,j,k-1/2}\right) \right]$$

The filter numerical flux vector is of the form

$$\widetilde{F}^{\star}_{i+1/2,j,k} = \frac{1}{2} R_{i+1/2,j,k} \phi^{\star}_{i+1/2,j,k} \tag{14}$$

where R is the right eigen vector matrix. The elements of $\phi^{\star}$ are denoted by $\phi^{l\star}$ and are given by

$$\phi^{l\star}_{i+1/2,j,k} = \kappa \theta^{l}_{i+1/2,j,k} \phi^{l}_{i+1/2,j,k} \tag{15}$$

The parameter κ is problem dependent and lies between 0.03 and 2 (Yee et al 1999). $\kappa = 1.0$ has been used in the simulations. The function $\theta^{l}_{i+1/2,j,k}$ is the Harten switch (Harten 1978). The formulation used for $\phi^{l}_{i+1/2,j,k}$ is given by the Harten–Yee upwind TVD form (Yee et al 1999).

C. Logarithm formulation of the continuity equation

When laser energy is added to a flow at rest, there is noticeable expansion at the core. This results in very small values of density at the core. When the continuity equation was advanced in time with density as the

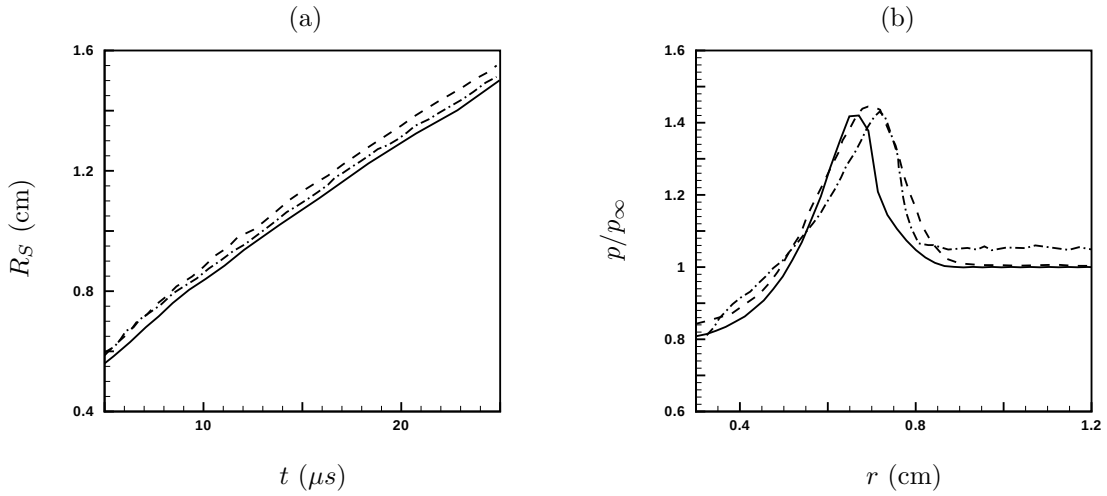

Figure 4. (a) Comparison of shock radius normal to the axis of the plasma, (b) Density profiles normal to the axis of the plasma at $10\ \mu s$ **——— : simulation results, — — — : experiment (Adelgren et al 2001), - - - - : simulations of Kandala and Candler (2003).**

dependent variable, the solution was found to become unstable. It was therefore decided to solve for the logarithm of density as the variable. Define

$$v = \log \rho \qquad \Rightarrow \qquad \rho = \mathrm{e}^v \tag{16}$$

The continuity equation becomes

$$\frac{\partial v}{\partial t} + u_i \frac{\partial v}{\partial x_i} = -\frac{\partial u_i}{\partial x_i}, \tag{17}$$

Note that ρ is always positive when computed as e^v, even for very small values of ρ. The $\log \rho$ formulation of the continuity equation therefore makes the solution stable in regions of very low density.

D. Validation Results

The solver with shock capturing and the $\log \rho$ formulation for the continuity equation is validated using a periodic shock tube problem and isotropic turbulence. Figure 2a shows instantaneous profiles of the solution for the periodic shock tube problem. A region of high density fluid is located at the center of a tube. This region is separated from low density regions of the same fluid on either side. The initial density jump is from 0.3 to 3 and viscosity in the problem is 0.005. The initial pressure profile is obtained from the ideal gas law, keeping temperature constant. This initial condition generates shock waves, which propagate in either direction. Density, pressure and temperature profiles obtained at $t = 1.0$ using shock capturing and the $\log \rho$ formulation are compared to those obtained without using these formulations. The profiles show good agreement.

Figure 2b shows decay of turbulent kinetic energy for isotropic turbulence. The initial velocity fluctuations are generated using Rogallo's (1981) method. The initial energy spectrum is top-hat, with energy in wave numbers between 8 and 16. The turbulent Reynolds number is 50 and the fluctuation Mach number is 0.3. Note that decay of turbulent kinetic energy in time with, and without the $\log \rho$ formulation of the continuity equation compare well.

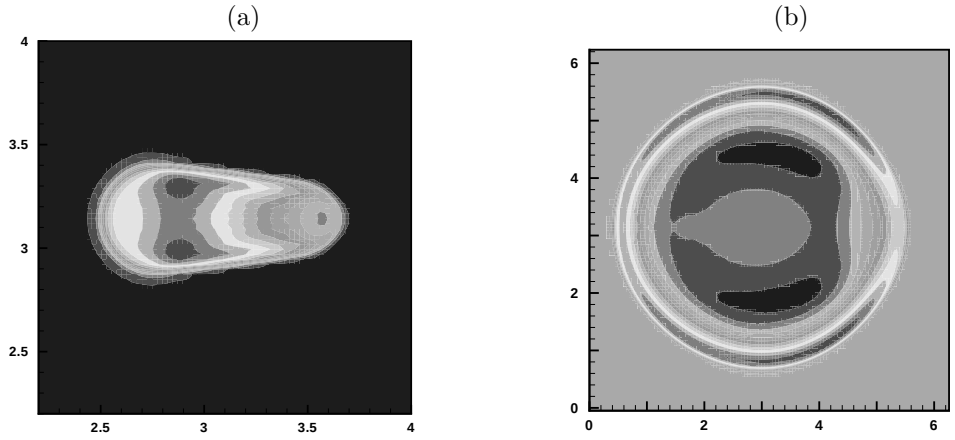

Figure 5. (a) Pressure contours at $t = 0.375\ \mu s$ show formation of a distinct shock wave normal to the axis of the plasma, (b) Pressure contours at $t = 20\ \mu s$ show that the blast wave is initially tear–drop shaped but become spherical in time.

III. Laminar plasma simulation

This section contains results from laminar simulations of the plasma. The source of the laser spark is an ND-YAG Laser with $532nm$ wavelength, $108mJ$ pulse energy and a pulse width of $20ns$. The laser beam radius is $10mm$ and the focal length is $100mm$. Experiments in laser induced breakdown (Adelgren et al 2001, Yan et al 2003) show that the plasma is initially tear–drop shaped. Figure 3a shows the axial temperature distribution that is used to model the initial temperature profile of the plasma. This is obtained from simulations of Kandala and Candler (2003) who model the initial laser energy deposition in detail. Laser energy deposition is assumed to be symmetric about the laser axis. The temperature profile normal to the plasma axis is assumed to be a Gaussian. Width of the laser spark normal to the plasma axis is obtained from the amount of laser energy absorbed by air. Figure 3b shows contours of temperature in a plane passing through the axis of the plasma.

1. Comparison to existing results

Figure 4a compares the shock radius normal to the plasma axis with experiment (Adelgren et al 2001) and simulation (Kandala and Candler 2003). Shock radius is defined by the outer edge of the pressure blast wave. Here the reference length scale l_r is obtained from the initial length of the plasma region to be 4.4075 mm and the reference velocity scale, c_r, is given by the background speed of sound. The reference time scale, t_r, is thus obtained to be 12.695 μs. The shock radius is seen to be slightly under–predicted. Figure 4b shows pressure profiles normal to the axis of the plasma. The computed pressure profile is observed to peak slightly behind the experimental profile. However, overall reasonable agreement is observed.

2. Shock formation and propagation

Laser energy is added into the flow by increasing the temperature at constant density. Thus sharp gradients in pressure are generated in the flow. The entire process can be divided into the formation and propagation of a shock wave. Formation of the shock wave is shown in figure 5a. Due to the tear–drop shape of the plasma, pressure gradients normal to the plasma axis are larger compared to the gradients along the plasma axis. Thus fluid elements in a region normal to the axis begin to gain kinetic energy and a shock wave begins

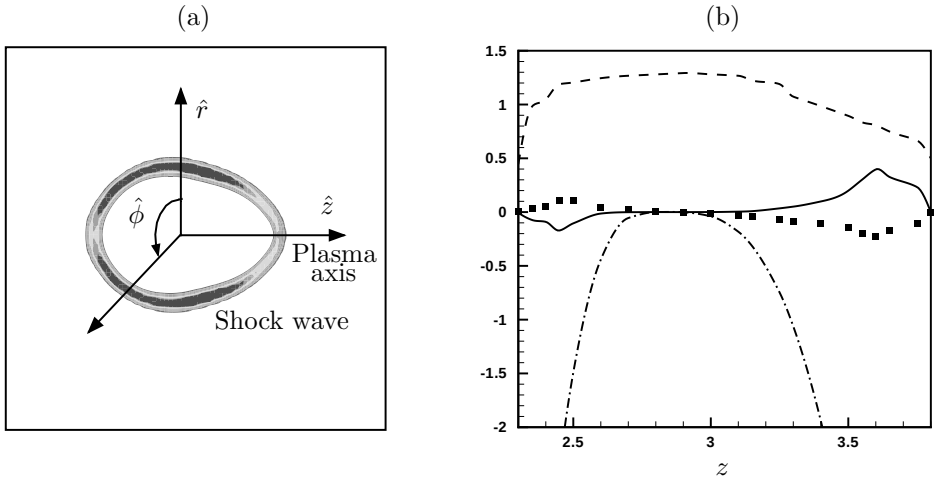

Figure 6. (a) Schematic showing propagation of a tear–drop shaped blast wave, (b) Generation of vorticity near leading and trailing edges of the plasma, ——— : vorticity jump across the shock wave, – – – – : shock strength, —·— : curvature of the shock front, ■ : tangential velocity measured ahead of the shock.

to form, and gradually steepens in intensity. The shock wave then propagates into the background gas with decreasing intensity. Figure 5b shows contours of pressure at an instant of time during propagation of the shock wave. The blast wave is initially tear–drop shaped as observed in figure 5a. The stronger pressure gradients normal to the plasma axis leads to larger acceleration of fluid elements in this direction. The effect is to push the blast wave faster normal to the plasma axis until pressure gradients in all directions become uniform and a nearly spherical blast wave propagates into the domain. Figure 5b shows that as the blast wave propagates to a radius 2 to 3 times the initial size of the plasma it becomes more and more spherical in shape.

3. Short time behavior

Baroclinic vorticity is observed to be generated near the leading and trailing edges of the plasma at times less than 5 μs. It is well known that shock waves with varying strength and curvature generate vorticity in the flow (Truesdell 1952, Lighthill 1957, Hayes 1957, Berndt 1966, Kevlahan 1997). A general expression for vorticity jump across an unsteady curved shock propagating into a two–dimensional non–uniform flow was

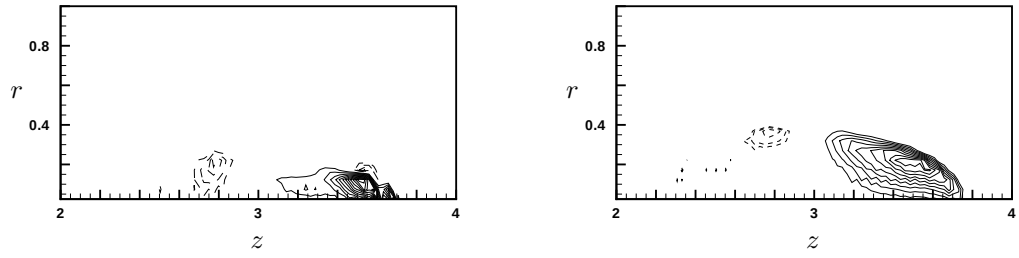

Figure 7. Contours of $\hat{\phi}$ component of vorticity at $t = 0.25$ μs and 1 μs, ——— : positive vorticity, – – – – : negative vorticity.

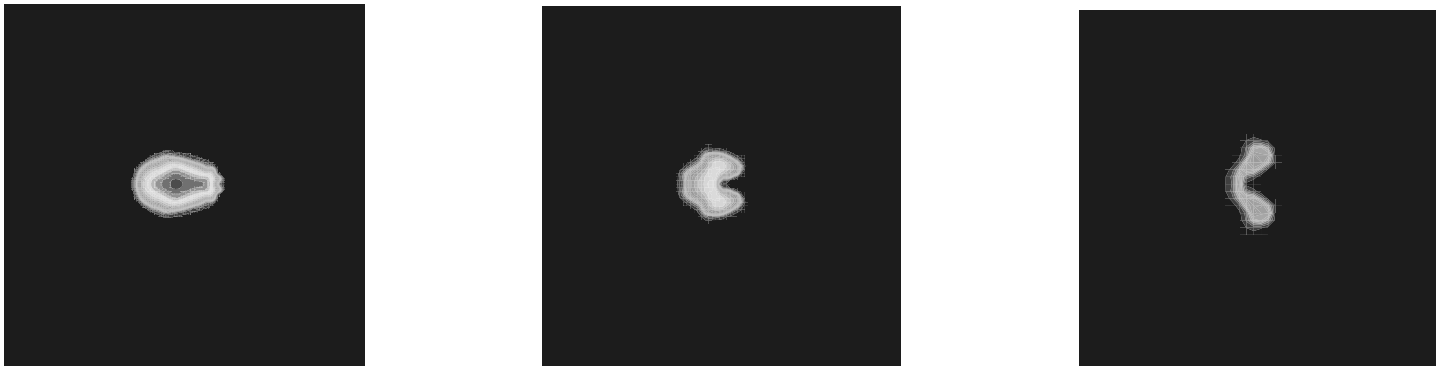

Figure 8. Temperature contours at $t = 18\ \mu s$, $30\ \mu s$ and $60\ \mu s$ show breaking and roll up of the temperature field.

derived by Kevlahan (1997). However a simpler expression for vorticity jump suggested by Truesdell (1952) has been used to explain generation of vorticity near the leading and trailing edges of the plasma. Truesdell considered vorticity jump across a two dimensional steady shock in uniform flow. The jump in vorticity was given by

$$\delta\omega = \frac{\mu^2}{1+\mu}\kappa U_t, \tag{18}$$

where κ is the curvature of the shock wave, U_t is the velocity tangential to the shock in the frame of reference of the shock wave, and μ is the shock strength given by

$$\mu = \frac{\rho_s}{\rho_\infty} - 1, \tag{19}$$

where ρ_s and ρ_∞ are the densities at the shock front, and ahead of it respectively. Note that vorticity has been considered to be positive, out of the plane of the paper.

Figure 6a shows a schematic for propagation of a tear–drop shaped shock wave. Note that both curvature and strength of the shock wave varies along its surface. Figure 6b shows the variation of shock strength, shock curvature, tangential velocity and jump in vorticity as a function of z at $t = 0.08$. The curvature of the shock wave is zero near the center, and attains large negative values near the edges of the plasma. The shock strength on the other hand, is maximum near the center and decreases towards the edges. The tangential velocity is negative and positive near the leading and trailing edges. The jump in vorticity as obtained from equation 18, is hence found to be positive and negative near the leading and trailing edges of the plasma, respectively.

The vorticity equation for a compressible, viscous flow with variable fluid properties can be written as

$$\begin{aligned}\frac{d\vec{\omega}}{dt} = & \underbrace{(\vec{u}\cdot\nabla)\vec{\omega}}_{\text{convection}} + \underbrace{(\vec{\omega}\cdot\nabla)\vec{u}}_{\text{vortex stretching/tilting}} - \underbrace{\vec{\omega}(\nabla\cdot\vec{u})}_{\text{bulk dilatation}} \\ & - \underbrace{\frac{\nabla p\times\nabla\rho}{\rho^2}}_{\text{baroclinic}} + \frac{1}{Re}\underbrace{(\nabla\times(\frac{1}{\rho}\nabla\cdot\tau))}_{\text{viscous}}.\end{aligned} \tag{20}$$

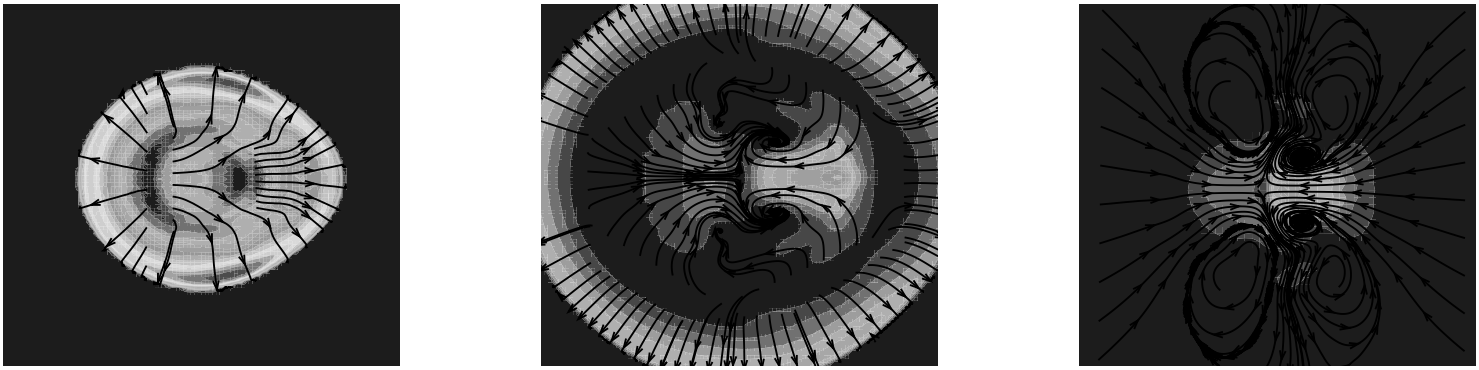

Figure 9. Velocity streamlines at $t = 4\ \mu s$, $12\ \mu s$ and $30\ \mu s$.

Since baroclinic vorticity is the only source term in equation 20, it is the only term responsible for initial generation of vorticity in the flow. Note that the flow is axisymmetric. Defining a cylindrical coordinate system along $\hat{r}$, $\hat{\phi}$ and $\hat{z}$ (figure 6a), any gradients in the flow will occur only along $\hat{r}$ and $\hat{z}$ directions. Thus the only possible component of baroclinic vorticity in the flow will be along $\hat{\phi}$.
Figure 7 shows contours of the $\hat{\phi}$ component of vorticity at subsequent instants of time. The contours are shown in a plane passing through the axis of the plasma. Positive and negative vorticity is observed near the leading and trailing edges of the plasma. Vorticity generation is stronger near the leading edge. The magnitude of vorticity is observed to decrease in time, as it spreads out further from the core of the plasma.

4. Long time behavior

This section shows evolution of the core of the plasma at times longer than $5\ \mu s$. Experiments in laser–induced break down (Adelgren 2001, Yan 2003) show that the core of the plasma eventually roll up generating a toroidal vortex ring. The time scale for this roll up depends on the amount of laser energy deposited in the flow. Experimental temperature measurements indicate that as a consequence of the roll up, the temperature field is advected such that the peak temperature shifts from the plasma axis to the center of the generated vortex ring.
Figure 8 shows long time evolution of the temperature field obtained in the simulations. Note that the temperature field starts breaking around $t = 18\ \mu s$ (figure 8a). The break up starts from the region of maximum temperature along the axis of the plasma. This propagates along the axis of the plasma from right to left resulting in formation of an axisymmetric temperature lobe around $30\ \mu s$ (figure 8b). In time this temperature lobe moves further away from the plasma axis and finally rolls up to form a toroidal vortex ring as shown in the contours of temperature at $60\ \mu s$ (figure 8c). Note that during this process, the maximum temperature is advected from the plasma axis to the center of the vortex ring.
The breaking and roll up of the temperature field can be explained by evolution of the velocity field in the core of the plasma. Figure 9 shows time evolution of the velocity field. Initially the core of the plasma expands. This is observed from velocity streamlines moving away from the plasma core (figure 9a). As the blast wave propagates away from the core, it can be shown, from conservation of mass that part of the fluid from the shock front moves back towards the plasma core. Thus a separating streamline is formed, ahead of which the fluid elements move away from the plasma core, but behind which a reverse flow is observed (figure 9b). The reverse flow is strongest along the plasma axis from right to left. Thus two jets of different

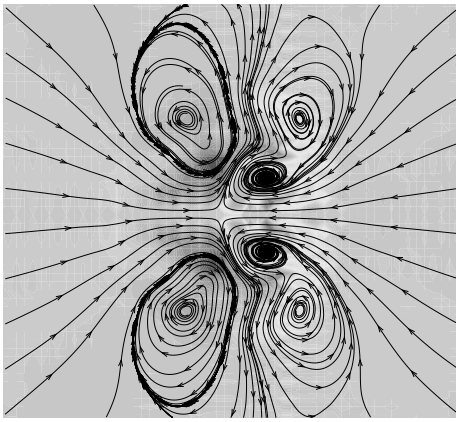

Figure 10. Velocity streamlines plotted over contours of vorticity magnitude at $30\ \mu s$**.**

velocity impinge head on along the plasma axis, yielding a complicated vorticity field (figure 9c). The fact that fluid rushes in from right to left along the plasma axis and then rolls over in a direction normal to the plasma axis leads to breaking and roll up of the temperature field.
Note that the actual vorticity field is much more complicated than just a single toroidal vortex ring. However the magnitude of vorticity is much stronger in the vortex ring closest to the plasma axis. This can be shown by plotting velocity streamlines over contours of vorticity magnitude (figure 10). Thus only a single toroidal vortex ring is observed in the experimental flow visualization.

IV. Plasma–turbulence interaction

Direct numerical simulation of isotropic turbulence was performed under conditions corresponding to past DNS by Blaisdell et al. (1991). The initial velocity fluctuations are isotropic and divergence–free, while initial fluctuations in pressure, temperature and density are assumed to be zero. The initial velocity fluctuations are generated using Rogallo's (1981) method. The Fourier coefficients of the initial velocity fields are given by

$$\hat{u} = \frac{\alpha k k_2 + \beta k_1 k_3}{k({k_1}^2 + {k_2}^2)^{1/2}} e_1 + \frac{\beta k_2 k_3 - \alpha k k_1}{k({k_1}^2 + {k_2}^2)^{1/2}} e_2 - \frac{\beta({k_1}^2 + {k_2}^2)^{1/2}}{k} e_3 \tag{21}$$

where

$$\alpha(k) = \frac{E(k)}{4\pi k^2}^{1/2} \mathrm{e}^{i\theta_1} \cos(\phi), \quad \beta(k) = \frac{E(k)}{4\pi k^2}^{1/2} \mathrm{e}^{i\theta_2} \cos(\phi). \tag{22}$$

Here θ_1, θ_2 and ϕ are random numbers from 0 to 2π, and e_i denote the unit vectors along the three coordinate directions.
The initial energy spectrum used in the simulations is a power four spectrum peaking at $k_0 = 5$. The initial flow field thus generated has an fluctuation Mach number $M_t = 0.3$ and turbulent Reynolds number $Re_\lambda = 50$. The turbulent field is allowed to decay for some time after which the velocity derivative skew–ness attains a steady value in the range of -0.3 to -0.4.

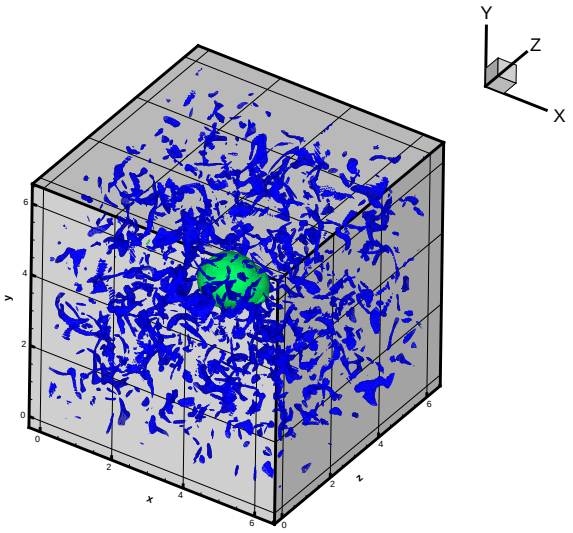

Figure 11. Instantaneous isosurfaces of velocity magnitude showing propagation of a blast wave through isotropic turbulence.

Laser energy is added to this flow by locally increasing the temperature and pressure at constant density. Figure 11 shows a schematic for the problem. Isosurfaces of velocity magnitude has been shown at a given instant of time. A tear–drop shaped blast wave is observed to propagate through the background turbulence. Interaction of this blast wave with the background turbulence and the effect of expansion in the plasma core has been described in this section.
Figure 12 shows propagation of the blast wave through background turbulence. Both side and sectional views have been shown for contours of density plotted at a given instant of time. A very strong blast wave is observed to propagate into the background compressing the turbulence, leaving the flow in the core to expand. The blast wave is initially strong and hence retains its tear drop shape. But the effect of the background turbulence is to dampen the blast wave intensity and soon it becomes weak enough to interact heavily with the turbulence and its shape gets distorted.

Compression across the blast wave and expansion in the plasma core affect turbulence levels in these regions. Note that the turbulence is statistically homogeneous in axisymmetric planes with respect to the plasma axis. Statistics were therefore computed in $z - r$ planes. Figure 13 shows statistics for turbulent kinetic energy, vorticity and divergence at $t = 1.9\ \mu s$. Note that in the vicinity of the blast wave turbulence levels get amplified due to presence of compression there. This trend is supported by linear analysis of turbulence interacting with a shock wave (Mahesh et al. 1995,1997). Also the expansion in the plasma core leads to suppression of turbulence levels there. Increase in viscosity due to high temperatures in the core also add to suppression of turbulence levels.
The extent of turbulence amplification across a shock wave would depend on the strength of the shock wave. Thus the extent of amplification should decrease in time as the shock wave propagates into the background with decreasing intensity. Figure 14a shows statistics for turbulent kinetic energy at $t = 1.9\ \mu s$, $2.25\ \mu s$ and $2.5\ \mu s$ plotted as a function of r at z corresponding to the center of the plasma. Note that the turbulence levels get suppressed in the plasma core. Also note that the amplification in turbulence levels across the shock wave decreases in time due to decreasing intensity of the shock wave. Figure 14b shows statistics for divergence in time. The two successive peaks indicate expansion in the core followed by compression

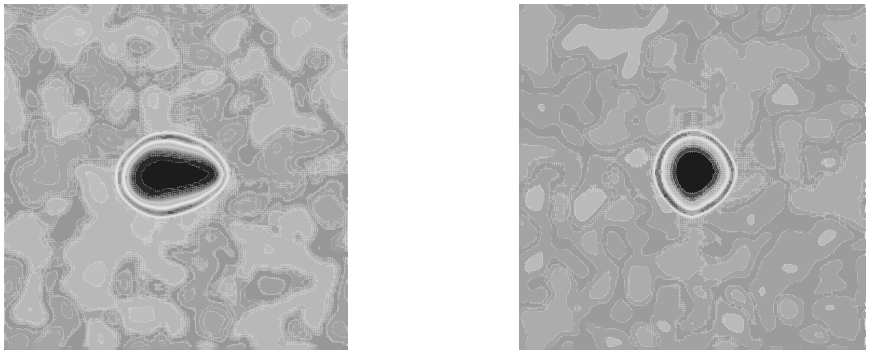

Figure 12. Contours of density at $t = 2.75\ \mu s$ showing propagation of a strong blast wave through the background turbulence.

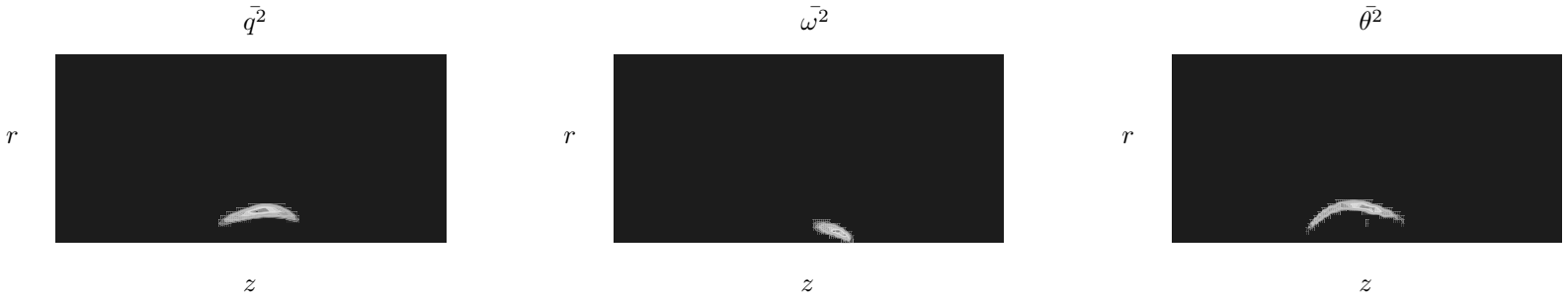

Figure 13. Statistics for turbulent kinetic energy, vorticity and divergence at $t = 1.9\ \mu s$.

across the blast wave. Note that at any given instant of time the effect of compression on the background turbulence is much more pronounced compared to the effect of expansion in the plasma core.

V. Summary

This paper uses direct numerical simulation to study the thermal effect of a region of plasma on quiescent air. The simulations solve the compressible Navier–Stokes equations using Fourier spectral methods. A shock capturing scheme is incorporated to account for the strong shock waves. Also, a logarithmic formulation for the continuity equation is developed to handle low densities at the core of the plasma. Both laminar and turbulent simulations for the plasma are conducted. For the laminar simulations, a tear–drop shaped blast wave propagates into the background becoming spherical in time. Shock radius and jumps in fluid properties at the shock front are compared to experiment and are found to agree reasonably. Both short and long time behavior of the plasma is studied. At short times, baroclinic vorticity is generated as a consequence of propagation of the curved shock through the domain. Generation of baroclinic vorticity has been explained based on Truesdell's relation (1952). At long times, the flow field rolls up leading to formation of toroidal vortex rings observed in experiments. This behavior of the flow field has been explained based on reverse flow behind the shock wave. For the turbulent simulations, turbulence levels get enhanced in regions of compression across the blast wave and suppressed in regions of expansion in the plasma core.

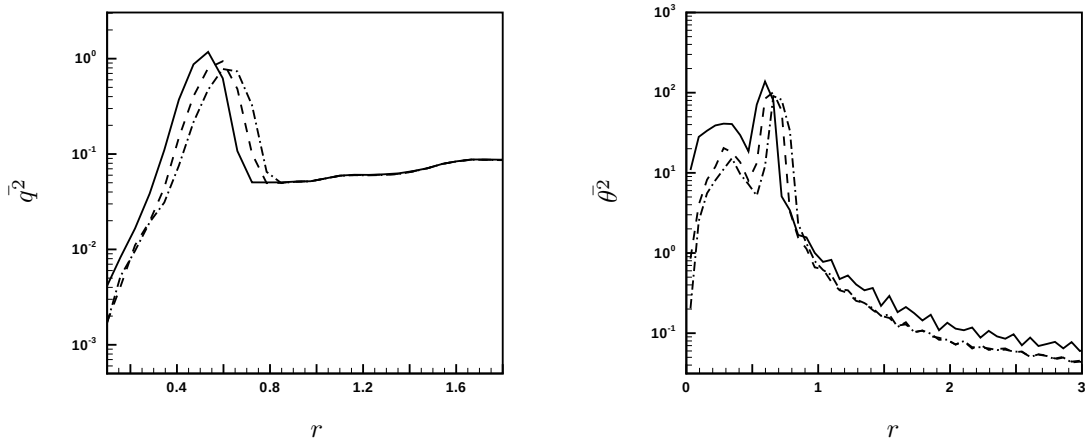

Figure 14. Statistics for turbulent kinetic energy and divergence at $t = 1.9$ μs, 2.25 μs and 2.5 μs.

Acknowledgments This work is supported by the United States Air Force Office of Scientific Research under grant FA-9550-04-1-0064. Computing resources were provided by the Minnesota Supercomputing Institute, the San Diego Supercomputing Center, and the National Center for Supercomputing Applications.

References

[1]R.G. Adelgren, H. Yan, G.S. Elliot, D. Knight, T.J. Beutner, A. Zheltovodov, M. Ivanov & D. Khotyanovsky, 2003, Localized flow control by laser energy deposition applied to Edney IV shock impingement and intersecting shocks, *AIAA paper 2003–31*.

[2]R. Adelgren, M. Boguszko & G. Elliott, 2001, Experimental summary report–shock propagation measurements for Nd:YAG laser induced breakdown in quiescent air, Department of Mechanical and Aerospace Engineering, Rutgers University.

[3]S.B. Berndt, 1966, The vorticity jump across a flow discontinuity, *J. Fluid Mech.*, **26**, 433–436.

[4]G.A Blaisdell, N.N. Mansour and W.C Reynolds, 1991, Numerical simulations of compressible homogeneous turbulence, Report No TF-50, Thermosciences Division, Department of Mechanical Engineering, Stanford University.

[5]H.L. Brode, 1955, Numerical solution of blast waves, *J. Appl. Phys.*, **26(6):** 766–775.

[6]E. Damon & R. Tomlinson, 1963, Observation of ionization of gases by a ruby laser, *Applied Optics*, **2(5)**.

[7]I. Dors, C. Parigger & J. Lewis, 2000, Fluid dynamic effects following laser–induced optical breakdown, *AIAA paper 2000–0717*.

[8]A. Harten, 1978, The artificial compression method for computation of shocks and contact discontinuities, *Math. Comp.* **32**, 363.

[9]W.D. Hayes, 1957, The vorticity jump across a gasdynamic discontinuity, *J. Fluid Mech.* **2**, 595–600.

[10]Z. Jiang, K. Takayama, K.P.B. Moosad, O. Onodera & M. Sun, 1998, Numerical and experimental study of a micro-blast wave generated by pulsed laser beam focusing, *Shock waves*, **8:** 337–349.

[11]R. Kandala & G. Candler, 2002, Computational modeling of localized laser energy deposition in quiescent air, *AIAA paper 2002–2160*.

[12]N. K. R. Kevlahan, 1997, The vorticity jump across a shock wave in a non–uniform flow, *J. Fluid Mech.* **341**, 371–384.

[13]J. Lewis, C. Parigger, J. Hornkohl &G. Guan, 1999, Laser–induced optical breakdown plasma spectra and analyses by use of the program NEQAIR, *AIAA paper 99–0723*.

[14]M.J. Lighthill, 1957, Dynamics of a dissociating gas, *J. Fluid Mech.* **2**, 1–32.

[15]K. Mahesh, S.K. Lele & P. Moin, 1995, The interaction of an isotropic field of acoustic waves with a shock wave, *J. Fluid Mech.*, **300:** 383–407.

[16]K. Mahesh, S.K. Lele & P. Moin, 1997, The influence of entropy fluctuations on the interaction of turbulence with a shock wave, *J. Fluid Mech.*, **334:** 353–379.

[17]P. Maker, R. Terhune & C. Savage, 1963, *Proccedings of the Third International Quantum Mechanics Conference*, Paris.

[18]R. Meyerand & A. Haught, 1963, Gas breakdown at optical frequencies, *Phys. Rev. Let.*, **11(9):** 401–403.

[19]P. Molina-Morales, K. Toyoda, K. Komurasaki & Y. Arakawa, 2001, CFD simulation of a 2–kW class laser thruster, *AIAA paper 2001–0650*.

[20]T. X. Phuoc, 2000, Laser spark ignition: Experimental determination of laser–induced breakdown thresholds of combustion gases, *Optics Communications* **175(4)**, 419–423.

[21]Y. P. Raizer, 1966, Breakdown and heating of gases under the influence of a laser beam, *Soviet Physics USPEKHI* **8(5)**, 650–673.

[22]Yu. P. Raizer, 1997, *Gas discharge physics*, 2nd edition, Springer–Verlag, New York.

[23]D. W. Riggins, H.F. Nelson & E. Johnson, 1999, Blunt-body wave drag reduction using focused energy deposition, *AIAA J.* **37(4)**, 460–467.

[24]R.S. Rogallo, 1981, Numerical experiments in homogeneous turbulence, *NASA Tech. Memo.* 81315.

[25]M.N. Scheider, S.O. Macheret, S.H. Zaidi, I.G. Girgis, Yu. P. Raizer & R.B. Miles, 2003, Steady and unsteady supersonic flow control with energy addition, *AIAA paper 2003–3862*.

[26]H. Steiner, W. Gretler & T. Hirschler, Numerical solution for spherical laser–driven shock waves, *Shock waves*, **8:** 337–349.

[27]C. Truesdell, 1952, On curved shocks in steady plane flow of an ideal fluid, *J. Aeronaut. Sci.* **19**, 826–828.

[28]T. S. Wang, Y.S. Chen, J. Liu, L.N. Myrabo & F.B. Mead, 2001, *AIAA paper 2001–0648*.

[29]H. Yan, M. Adelgren, M. Bouszko, G. Elliott & D. Knight, 2003, Laser energy deposition in quiescent air, *AIAA paper 2003–1051*.

[30]H.C. Yee, N.D. Sandham & M.J. Djomehri, 1999, Low–dissipative high–order shock–capturing methods using characteristic-based filter, *J. Comput. Phys.* **150**, 199–238.